iScience

CellPress
OPEN ACCESS

Article

Mapping and tracing Grem1^{+} stromal cells in an *Apc*$^{Min/+}$ mouse utilizing cryopreserved intestinal sections prepared via modified Swiss-roll technique

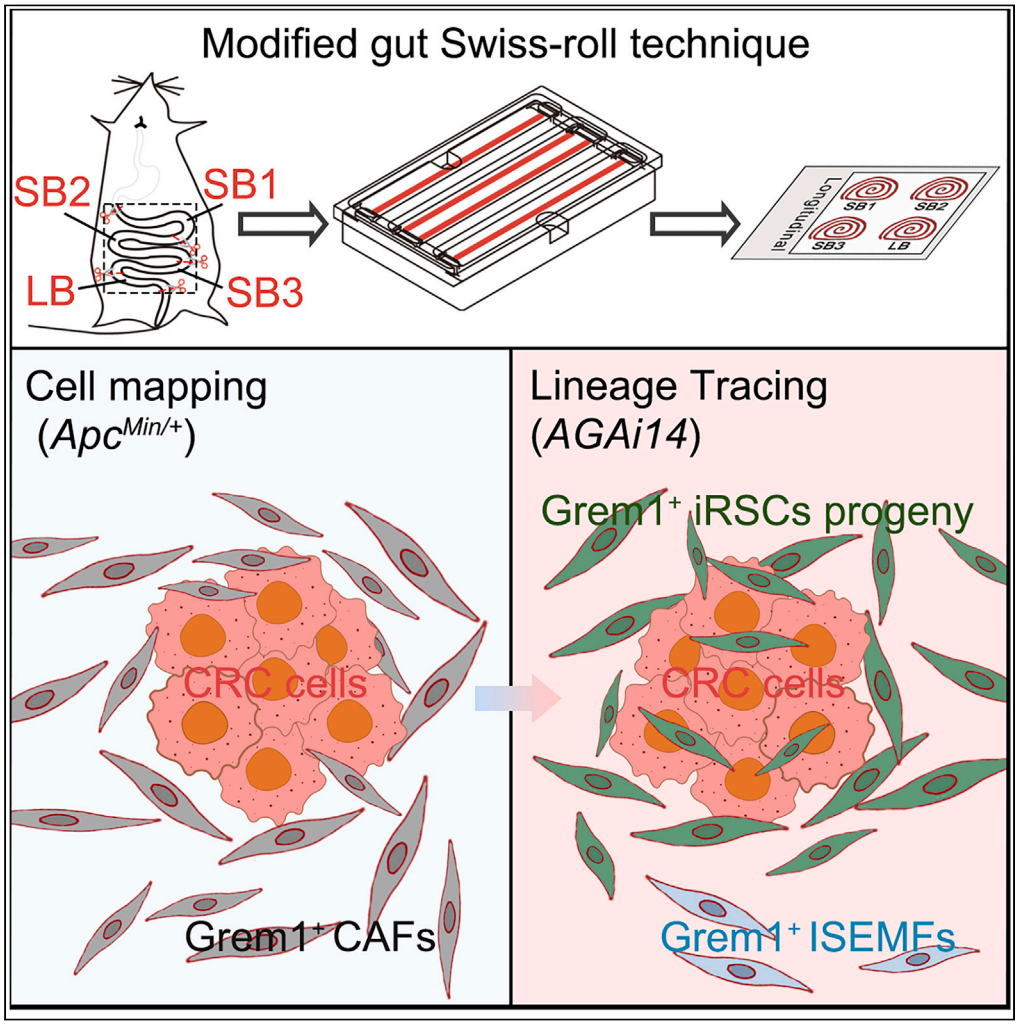

Youheng Jiang, Zhang Fu, Yanfang Chen, ..., Qingyuan Zhang, Qi Zhang, Ningning Li

heyulong@mail.sysu.edu.cn (Y.H.)
zhangqy33@mail2.sysu.edu.cn (Q.Z.)
zhangqi2@sysush.com (Q.Z.)
linn29@mail.sysu.edu.cn (N.L.)

Highlights

Design of a custom mold to modify gut Swiss-roll technique for comprehensive staining

Grem1^{+} CAFs increase markedly within *Apc*$^{Min/+}$ mouse tumors compared to normal mucosa

Most Grem1^{+} CAFs infiltrating the tumor core are originated from Grem1^{+} iRSCs

Minor Grem1^{+} CAFs distributed in submucosa retain characteristics of Grem1^{+} ISEMFs

Jiang et al., iScience 27, 111173
November 15, 2024
https://doi.org/10.1016/j.isci.2024.111173

iScience

CellPress
OPEN ACCESS

Article

Mapping and tracing Grem1^{+} stromal cells in an *Apc*$^{Min/+}$ mouse utilizing cryopreserved intestinal sections prepared via modified Swiss-roll technique

Youheng Jiang,[1,2,9] Zhang Fu,[1,3,9] Yanfang Chen,[2,9] Qunlong Jin,[1,2,9] Yanming Yang,[1] Zerong Lin,[1] Changxue Li,[1,2] Yunfei Gao,[1,4] Zepeng Dong,[1] Yang He,[5] Xinjun Mao,[6] Yulong He,[1,2,*] Qingyuan Zhang,[2,*] Qi Zhang,[7,*] and Ningning Li[1,8,10,*]

SUMMARY

Grem1^{+} cancer-associated fibroblasts (CAFs) are crucial in colorectal cancer (CRC) development, yet technical challenges have limited understanding of their origins, spatiotemporal distribution, and potential roles. Here, we devised a custom mold, optimizing the gut Swiss-roll technique to create a single cryopreserved slide for comprehensive staining. Our integrated approach uncovered a marked increase in Grem1^{+} CAFs within *Apc*$^{Min/+}$ mouse tumors at 12 weeks, compared to normal mucosa. Subsequent lineage tracing in *Grem1-CreER*^{T2}*; R26-LSL-tdTomato; Apc*$^{Min/+}$ mice revealed that most Grem1^{+} CAFs infiltrating the tumor core originated from Grem1^{+} intestinal reticular stem cells (iRSCs). A minor subset of Grem1^{+} CAFs, located in the submucosa, retained characteristics of Grem1^{+} intestinal sub-epithelial myofibroblasts (ISEMFs). Altogether, CAFs derived from Grem1^{+} iRSCs may serve as a principal stromal cell type driving early-stage CRC progression, while Grem1^{+} ISEMFs contribute less from a more distant location. Hence, targeting Grem1^{+} CAFs presents an early and promising therapeutic strategy in CRC.

INTRODUCTION

Colorectal cancer (CRC) stands as a formidable challenge in the realm of oncology, representing one of the leading causes of cancer-related morbidity and mortality globally.[1] The intricate interplay between tumor cells and the tumor microenvironment (TME) plays a pivotal role in determining the trajectory of CRC progression.[2] Within this dynamic TME, cancer-associated fibroblasts (CAFs) serve as key players, not only contributing significantly to tumor growth, invasion, and therapy resistance, but also modulating immune responses and angiogenesis.[3–5] Given the heterogeneity and plasticity of CAFs,[6,7] the mechanisms through which CAFs regulate the TME are diverse and not fully understood.

Gremlin-1 (Grem1), a secreted cysteine knot protein, classically interacts with BMP dimers, inhibiting the activation of BMP type I and II receptors.[8,9] Recent studies have revealed its novel role as a cytokine, capable of interacting with non-BMP partners, such as the vascular endothelial growth factor receptor,[10] epidermal growth factor receptor,[11] and fibroblast growth factor receptor,[12] highlighting the multifaceted influence of Grem1 in cancer progression. Among the heterogeneous population of CAFs, Grem1^{+} stromal cells have emerged as a subset of CAFs, potently modulating CRC progression.[13,14] However, the origins/progenitors of Grem1^{+} CAFs within the TME remain largely unknown, presenting a critical gap in our understanding of their impact on CRC development and offering a potential target for therapeutic interventions.

Transgenic mouse models are crucial for conducting lineage tracing experiments.[15,16] In murine gastrointestinal research, particularly within oncological[17] and inflammatory disease studies,[18] the Swiss-roll technique is a valuable method. This technique allows for a comprehensive examination of extensive intestinal sections, thereby significantly enhancing the efficiency in detecting and analyzing multiple pathologic lesions or disease foci.[19,20] However, the existing Swiss-roll techniques have several limitations. First, previous studies have primarily

[1]Tomas Lindahl Nobel Laureate Laboratory, The Seventh Affiliated Hospital of Sun Yat-sen University, Shenzhen 518107, China
[2]Digestive Diseases Center, Guangdong Provincial Key Laboratory of Digestive Cancer Research, The Seventh Affiliated Hospital of Sun Yat-sen University, Shenzhen 518107, China
[3]Department of Geriatrics, The Seventh Affiliated Hospital of Sun Yat-Sen University, Shenzhen 518107, China
[4]Department of Otolaryngology, The Seventh Affiliated Hospital of Sun Yat-sen University, Shenzhen 518107, China
[5]School of Mechanical Engineering and Automation, Harbin Institute of Technology, Shenzhen 518107, China
[6]Department of Anesthesiology, The Affiliated Hospital of Youjiang Medical University for Nationalities, Baise 533000, China
[7]Department of Anesthesiology, The Seventh Affiliated Hospital of Sun Yat-sen University, Shenzhen 518107, China
[8]China-UK Institute for Frontier Science, Shenzhen 518107, China
[9]These authors contributed equally
[10]Lead contact
*Correspondence: heyulong@mail.sysu.edu.cn (Y.H.), zhangqy33@mail2.sysu.edu.cn (Q.Z.), zhangqi2@sysush.com (Q.Z.), linn29@mail.sysu.edu.cn (N.L.)
https://doi.org/10.1016/j.isci.2024.111173

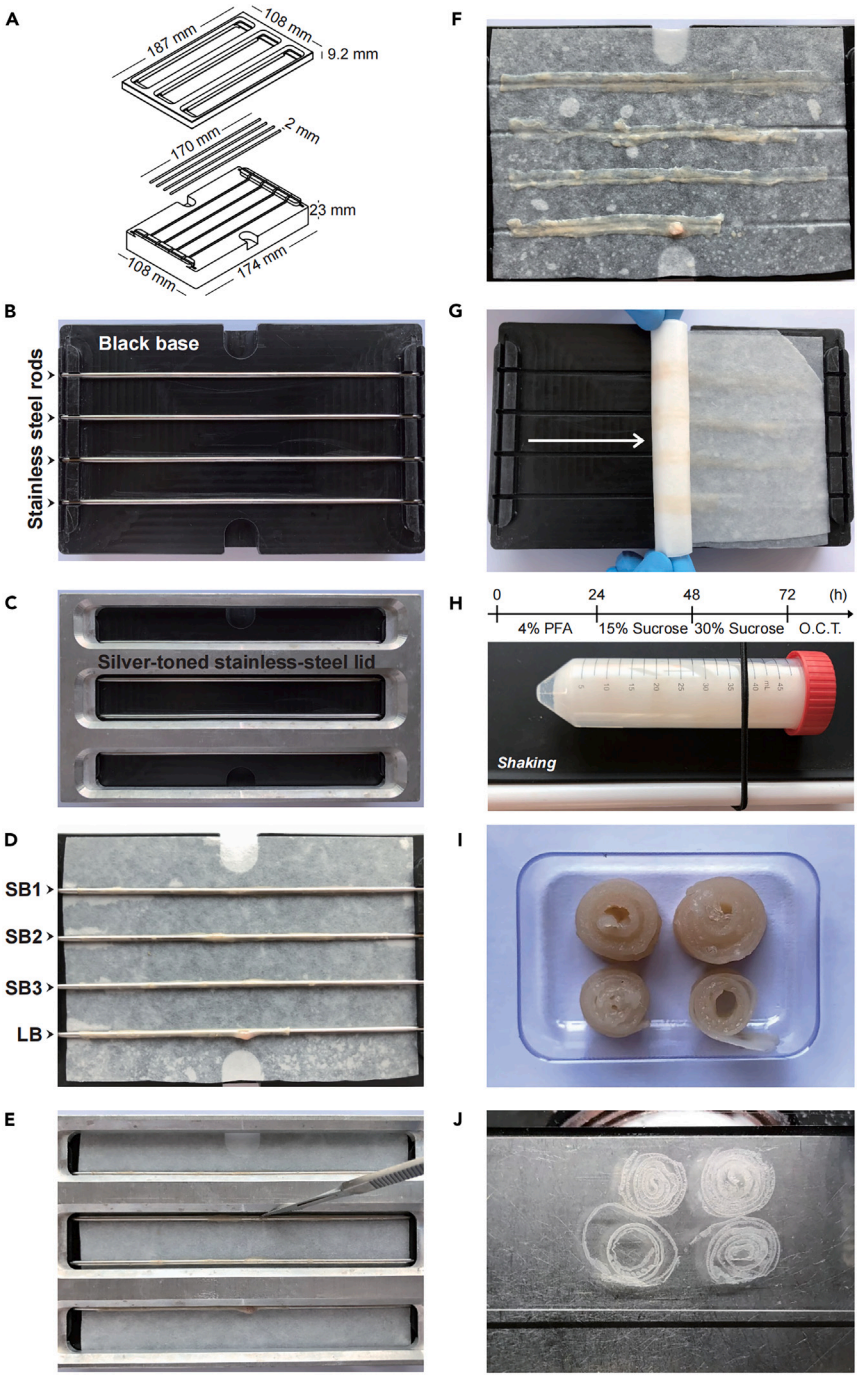

Figure 1. Design of a mouse intestinal longitudinal cutting mold for frozen tissue sections

(A) This design diagram details a specialized mold engineered for the precise longitudinal cutting of murine intestinal specimens, including dimensions for length, width, height, and diameter.

(B) Top view of the four stainless steel rods positioned on the black base.

(C) Top view of the silver lid aligned on the black base, a crucial step for ensuring the stability of cutting.

(D) The intestinal tract is segmented into three equal lengths for the small intestine (SB1, SB2, SB3) and one for the large intestine (LB). Each intestinal segment is carefully threaded onto stainless steel rods and then anchored onto the black base.

(E) A scalpel is used to perform a longitudinal incision along the intestine, positioned against the lateral wall of the silver lid, enabling a smooth and controlled cut.

(F) The intestines are carefully spread out and placed flat on absorbent paper after the removal of the stainless-steel rods.

(G) To encase the intestinal tissues, they were topped with another absorbent paper and then rolled directed by the white arrow.

Figure 1. *Continued*

(H) Intestinal rolls wrapped in absorbent paper are secured in a 50-mL centrifuge tube containing 4% PFA, where they are shaken for 24 h to ensure thorough fixation. The process continues with a graduated dehydration in 15% and 30% sucrose solutions before O.C.T. embedding, as delineated in the timeline.

(I) The four coiled intestinal segments are sequentially placed in the embedding cassette, ready for further O.C.T. embedding process.

(J) Frozen tissue sections are mounted onto glass slides to create a complete frozen slide of the mouse's entire intestine for further staining.

utilized dissecting scissors for intestinal incisions,[19,21] which require considerable expertise and often result in serrated edges. Second, it is standard practice to prepare four separate tissue blocks from the four intestinal rolls of a single mouse, a procedure that is both time-consuming and labor-intensive. Third, the preparation of intestinal Swiss rolls typically involves embedding the tissue in paraffin.[22] This process, which includes dehydration and high-temperature wax immersion, may potentially damage certain proteins and antigens within the tissue, thereby compromising the quality of immunofluorescence (IF) staining.

Here, we developed an enhanced Swiss-roll technique with a tailored mold to longitudinally section and mount the entire gut on a singular cryopreserved slide, which significantly improves its utility and accuracy for dye and IF staining. Harnessing these integrated methods, we performed tempo-spatial distribution and fate mapping analyses of Grem1$^+$ cells, in *Apc*$^{Min/+}$ and *Grem1-CreER*^{T2}; *R26-LSL-tdTomato*; *Apc*$^{Min/+}$ mouse models, respectively. We observed that Grem1$^+$ CAFs were more abundant within tumor regions. Remarkably, the majority of Grem1$^+$ CAFs were descendants of Grem1$^+$ intestinal reticular stem cells (iRSCs),[23] and located throughout the entire tumor region. Intriguingly, a small subset of Grem1$^+$ CAFs, although not derived from iRSCs, was primarily distributed in the submucosal area and exhibited characteristics of intestinal sub-epithelial myofibroblasts (ISEMFs),[24] constituting a repertoire of distributionally disparate yet functionally subsidiary communities of Grem1$^+$ CAFs.

RESULTS

Design of a mouse intestinal longitudinal cutting matrix for frozen tissue sections

To overcome traditional dissection inefficiencies and optimize murine intestinal tissue preparation for histological analysis, we developed a mold, the "Mouse Intestinal Longitudinal Cutting Matrix" (Figures 1A and S1). This mold, comprising a black base, a silver-toned stainless-steel lid, and four stainless steel rods, provides a stable platform for precise sectioning (Figures 1B and 1C).

We extracted the intestinal tract, purged its contents using ice-cold phosphate buffered saline (PBS), and segmented it into three equal lengths for the small intestine (SB1, SB2, SB3) and one for the large intestine (LB). The intestinal segments were then threaded onto the mold's stainless-steel rods (Figure 1D). An incision was made along the length of the intestine (Figure 1E), and ice-cold PBS was applied to flatten the tissue edges (Figure 1F). We also evaluated the traditional method of using scissors for intestinal incisions and found that it frequently resulted in serrated edges, particularly among less experienced practitioners (Figure S2A). In contrast, our custom-designed device consistently yielded intestines with neatly trimmed edges (Figure S2B). Our mold streamlines the sectioning process, ensuring precision, reproducibility, and uniformly flat edges for histological examination.

Following sectioning, the intestinal tissue was rolled (Figure 1G), fixed in 4% paraformaldehyde (PFA), dehydrated in sucrose solutions (Figure 1H), and tightly coiled for embedding. The coiled tissues were arranged in a tissue embedding cassette (Figure 1I) and encased in optimum cutting temperature (O.C.T.) compound. The frozen tissue block was then sectioned and mounted on an adhesive slide (Figure 1J), ready for staining and analysis. This process enables the mounting of the entire murine intestine onto a single slide, facilitating comprehensive histological examination.

Dye and immunofluorescence staining of gut tissue samples prepared using our enhanced Swiss-roll technique

We validated the efficacy of our enhanced Swiss-roll technique for gut tissue preparation using various histological staining methods, beginning with hematoxylin and eosin (H&E). The yielded sections exhibited distinct nuclear (blue) and cytoplasmic (pink) staining, exemplifying the classical quality of H&E-stained tissues (Figure 2A). These images facilitated measurements of key morphological parameters such as villus length and crypt depth. Next, we applied Alcian blue-periodic acid Schiff (AB-PAS) staining, with blue indicating acidic mucins and glycoproteins, and pink to red identifying neutral mucins and collagen, effectively highlighting mucins and carbohydrates critical to understanding tissue pathology.[25,26] The coloration demonstrated that our protocol preserved the integrity of these substances (Figure 2B), ensuring suitability for detailed histochemical studies. Further, our Swiss-roll sections also proved compatible with IF staining. For example, precise localization of E-cadherin (green) distinguished epithelial from stromal cells within the gut, including tumor areas (Figure 2C). The natural fidelity of antigen preservation and the clarity of fluorescent labeling attested to the high quality of the tissue samples prepared with our method. Lastly, panoramic imaging combined with our technique, provided comprehensive visualization of the entire intestinal architecture from SB1 to LB (Figure S3), facilitating exhaustive histopathological assessments, such as tumor burden evaluation in the *Apc*$^{Min/+}$ mouse model.

Increased abundance of Grem1$^+$ stromal cells in tumor regions of *Apc*$^{Min/+}$ mice at 12 weeks

Apc$^{Min/+}$ (adenomatous polyposis coli multiple intestinal neoplasia) mice, widely utilized for studying intestinal tumorigenesis, harbor a mutation in the *APC* gene, a tumor suppressor gene frequently mutated in both familial and sporadic forms of CRC in humans.[27] Utilizing our refined Swiss-roll technique for gut tissue preparation and multi-fluorophore labeling, we delineated the spatial distribution of Grem1$^+$ cells within the TME of the *Apc*$^{Min/+}$ mouse model at 12 weeks of age, a time point reflective of mid-stage intestinal tumor development. IF staining identified Grem1$^+$ cells and their spatial distribution within the TME, using vimentin as a mesenchymal marker (Figures 3A–3C) and E-cadherin

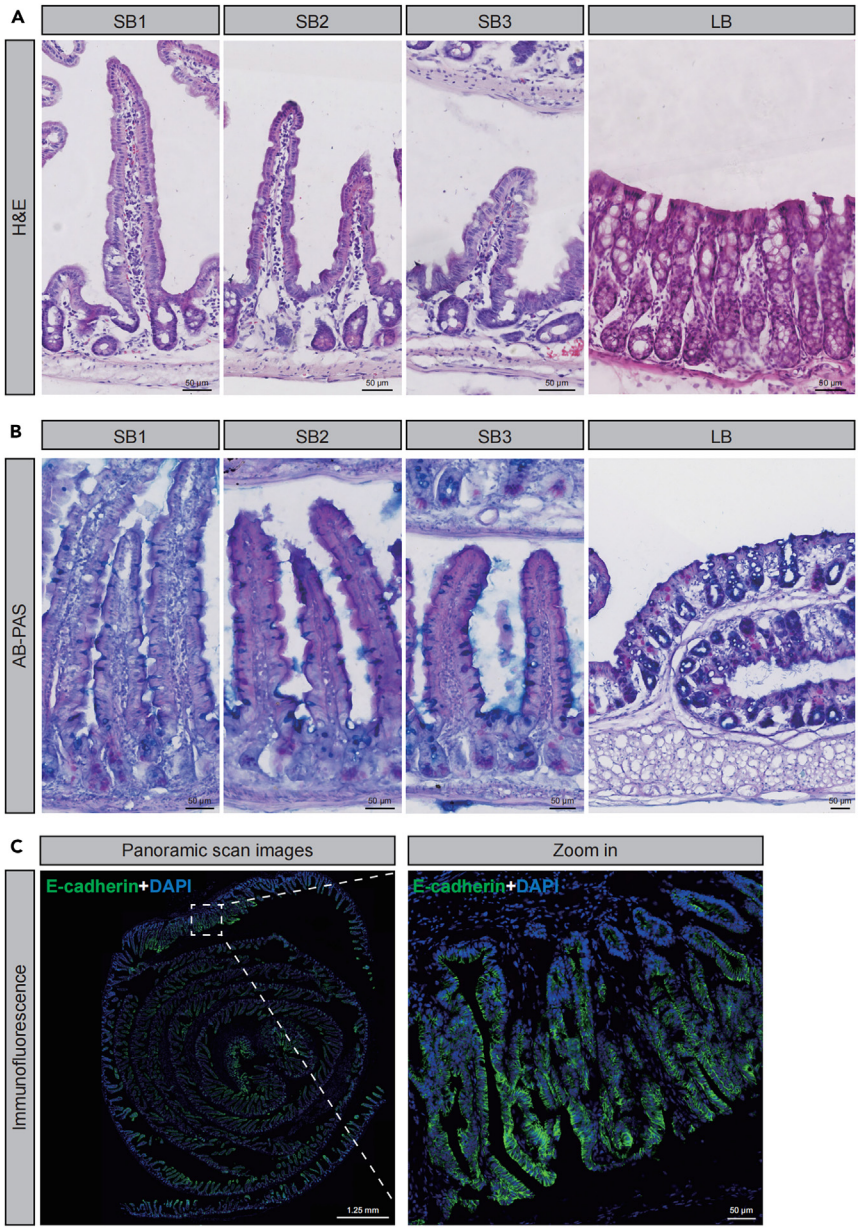

Figure 2. Enhanced quality of frozen intestinal tissue sections stained with dye and immunofluorescence (IF)

(A) Representative H&E staining displays the intestinal segments SB1 to LB, illustrating the preservation of morphology, attesting to our refined tissue preparation technique. Scale bar: 50 μm.

(B) Representative AB-PAS staining sections from SB1 to LB reveal mucin and carbohydrate profiles, confirming the effectiveness of our enhanced tissue preparation method. Scale bar: 50 μm.

(C) Representative IF images demonstrate E-cadherin (green) in the $Apc^{Min/+}$ mouse gut, with DAPI counterstaining (blue). A panoramic scan and detailed zoom-in emphasize E-cadherin's distribution, as demarcated by white dashed boxes. Scale bars: 1.25 mm (panoramic), 50 μm (zoom-in).

as an epithelial marker (Figure 3E). In the normal areas (regions without tumors), we observed a low number of $Grem1^+$ cells, which were primarily distributed below the small intestinal isthmus (*Sii*),[23] not extending toward the villus tips (Figure 3A). In contrast, tumor regions showed an increased abundance of $Grem1^+$ cells that extended beyond the *Sii* toward the villus tips (Figures 3B and 3C). Notably, a significant majority of these $Grem1^+$ cells in the tumor regions expressed vimentin (95.63%), with only a minor portion (4.37%) being $vimentin^-$ (Figure 3D, $p < 0.0001$; Table S1), while most were $E\text{-}cadherin^-$ (Figures 3E and 3F, $E\text{-}cadherin^+$ vs. $E\text{-}cadherin^-$ = 5.53% vs. 94.47%, $p < 0.0001$; Table S2). These findings suggest an increased presence of $Grem1^+$ stromal cells in the tumor milieu at the intermediary stage of invasive tumor progression. However, the origins of this distinct $Grem1^+$ stromal cell population warrant further investigation.

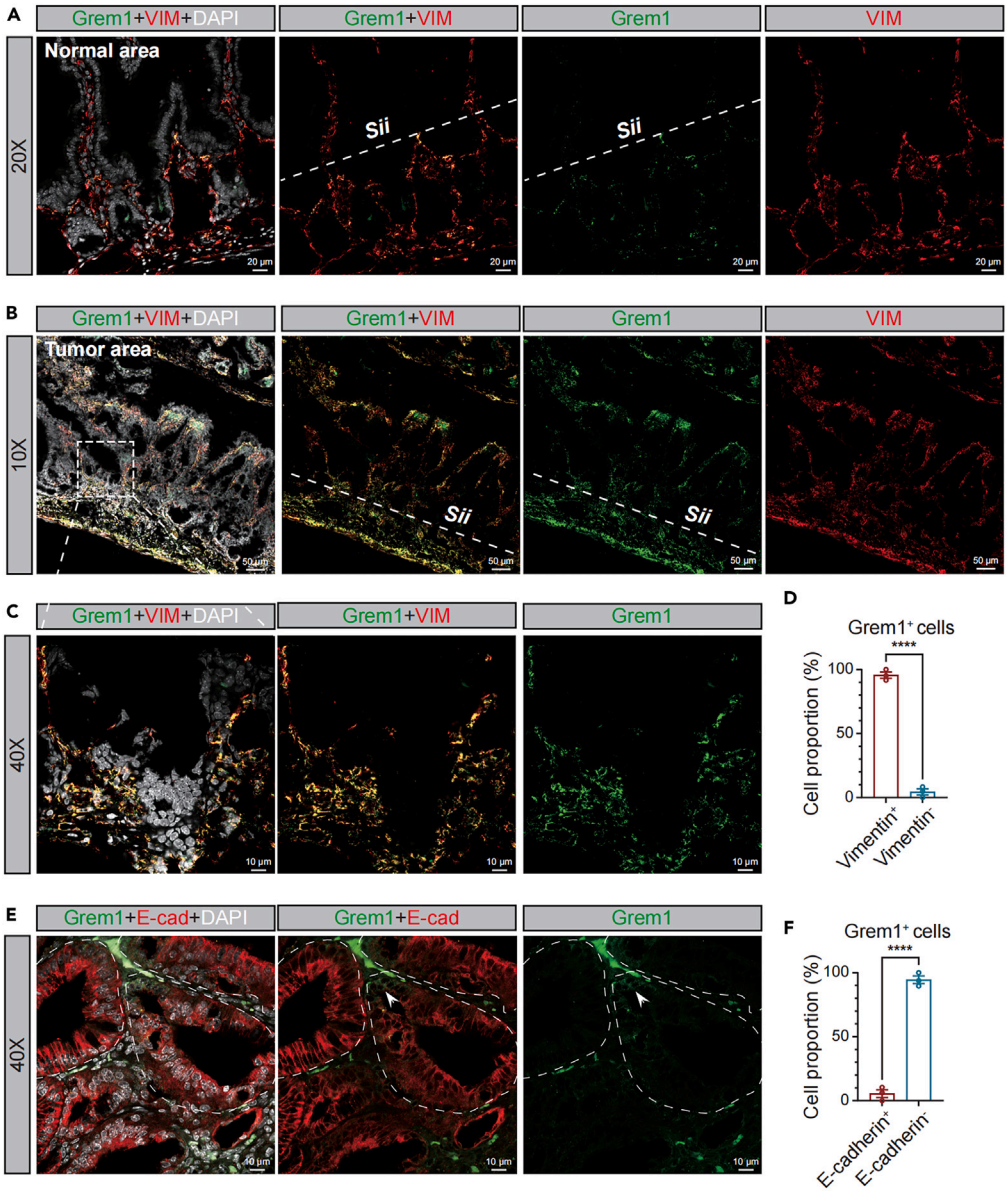

Figure 3. Increased abundance of Grem1$^+$ stromal cells in tumor regions of *Apc$^{Min/+}$* mice at 12 weeks

(A) Representative IF staining at 20X magnification for Grem1 (green), vimentin (red) and DAPI (white) in the normal area of 12-week-old *Apc$^{Min/+}$* mice. The small intestinal isthmus (*Sii*) is demarcated by white dashed lines. Scale bars: 20 μm.

(B and C) Representative IF staining at 10X (B) and 40X (C) magnification for Grem1 (green), vimentin (red), and DAPI (white) in the tumor area of 12-week-old *Apc$^{Min/+}$* mice. A white dashed box (B) outlines the area enlarged to 40X magnification (C). Scale bars: 50 μm (B) and 10 μm (C).

(D) Quantitative analysis detailing the percentage of Grem1$^+$ cells that are either Vimentin$^+$ or Vimentin$^-$ within the tumor region, using 40X magnification images from intestinal sections of three *Apc$^{Min/+}$* mice. Statistical significance is assessed using a two-tailed unpaired t-test, with **** denoting $p < 0.0001$. Data are presented as the mean ± standard error of the mean (SEM).

(E) Representative IF staining at 40X magnification for Grem1 (green), E-cadherin (red) and DAPI (white) in the tumor area of 12-week-old *Apc$^{Min/+}$* mice. The irregular white dashed circle outlines the morphology of the epithelial region, and white arrows highlight Grem1$^+$ epithelial tumor cells with lower Grem1 expression compared to Grem1$^+$ stromal cells. Scale bars: 10 μm.

(F) Quantitative analysis detailing the proportion of Grem1$^+$ cells that are either E-cadherin$^+$ or E-cadherin$^-$ within the tumor region, based on 40X magnification images from intestinal sections of three *Apc$^{Min/+}$* mice. Statistical significance is assessed using a two-tailed unpaired t-test, with **** denoting $p < 0.0001$.

Tracing the origins of Grem1$^+$ stromal cells in *Apc$^{Min/+}$* mice

To elucidate the origins of Grem1$^+$ stromal cells, we established a triple transgenic mouse model by interbreeding *Apc$^{Min/+}$*, *Grem1-CreER^{T2}*, and *R26-LSL-tdTomato (Ai14)* mice (Figure 4A), which were termed the *AGAi14* model, facilitating real-time visualization and tracking of

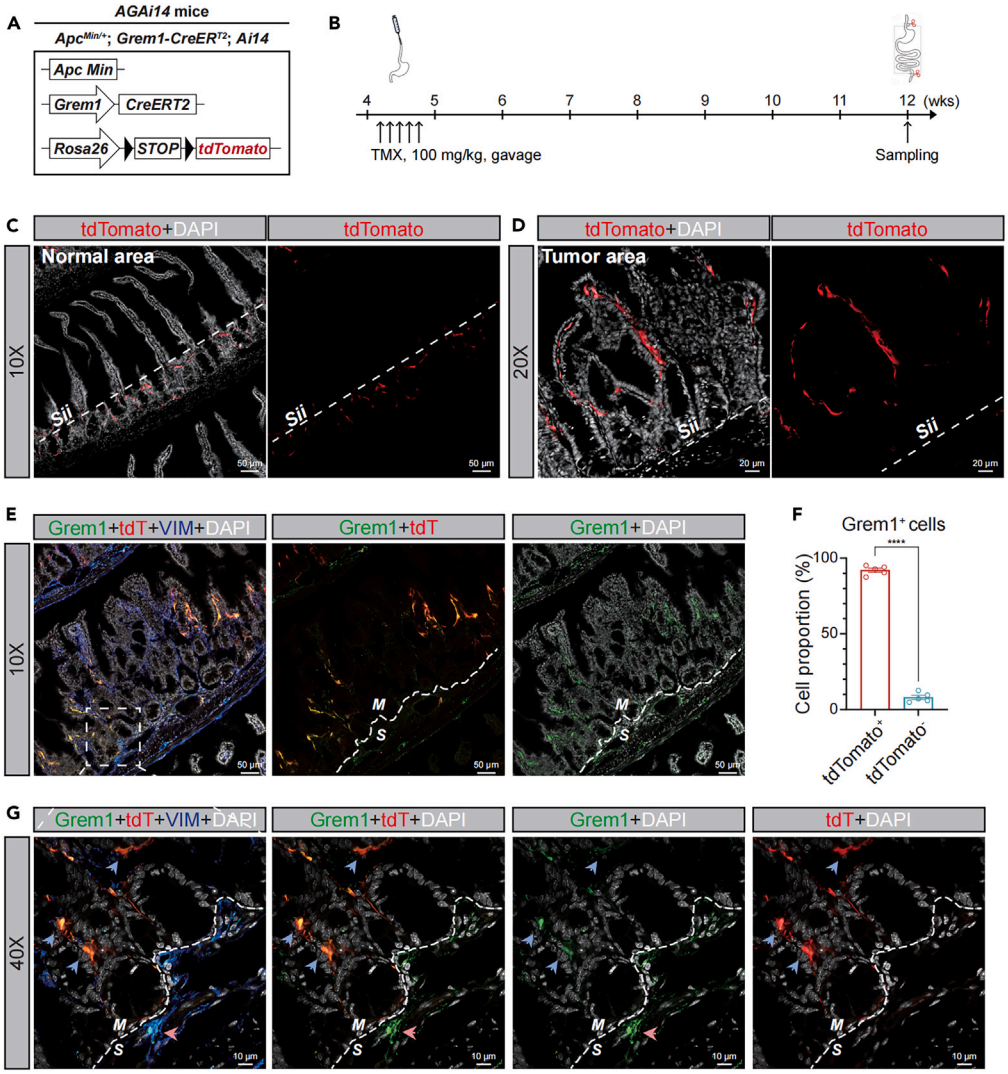

Figure 4. Tracing the origins of Grem1$^+$ stromal cells in *Apc*$^{Min/+}$ mice

(A) Schematic diagram illustrating the generation of the *AGAi14* mouse model by intercrossing *Apc*$^{Min/+}$, *Grem1-CreER*^{T2}, and *R26-LSL-tdTomato* (*Ai14*) mice. The individual mouse lines and Cre/*LoxP* recombination modules are outlined.

(B) Experimental timeline depicting the administration of tamoxifen (abbreviated as TMX) via gavage at a dosage of 100 mg/kg to 4-to-5-week-old *AGAi14* mice across five consecutive days. The timeline marks the weeks (wks) post-administration, with tissue sampling conducted at 12 weeks of age.

(C) Representative IF staining at 10X magnification for tdTomato (red) and DAPI (white) in the normal area of 12-week-old *AGAi14* mice. The *Sii* is demarcated by white dashed lines. Scale bars: 50 μm.

(D) Representative IF staining at 20X magnification for tdTomato (red) and DAPI (white) in the tumor area of 12-week-old *AGAi14* mice. Scale bars: 20 μm.

(E) Representative IF staining at 10X magnification for Grem1 (green), tdTomato (red), vimentin (blue) and DAPI (white) in the tumor area of 12-week-old *AGAi14* mice. Co-localization of Grem1 (green) and tdTomato (red) appears orange, indicating of tdTomato$^+$/Grem1$^+$ cells. A white dashed box outlines the area enlarged to 40X magnification in panel G. White dashed lines clearly define the interface between the mucosal (*M*) and submucosal (*S*) layers within the tumor area. Scale bars: 50 μm.

(F) Quantitative analysis detailing the proportion of Grem1$^+$ cells that are either tdTomato$^+$ or tdTomato$^-$ within the tumor region, based on 40X magnification images from intestinal sections of five *AGAi14* mice. Statistical significance is assessed using a two-tailed unpaired t-test, with **** denoting $p < 0.0001$. Data are presented as the mean ± SEM.

(G) Representative IF staining at 40X magnification for Grem1 (green), tdTomato (red), vimentin (blue) and DAPI (white) in the tumor area of 12-week-old *AGAi14* mice. tdTomato$^-$/Grem1$^+$ stromal cells in the submucosal layer are identified by pink arrows, whereas tdTomato$^+$/Grem1$^+$ cells in the mucosal layer are denoted by blue arrows. Scale bar: 10 μm.

Grem1$^+$ cells within the evolving tumor landscape. Previous research by Worthley et al. established that Grem1$^+$ iRSCs are a primary source of Grem1 in the gut under normal conditions.[23] At 4 weeks of age, corresponding to the initial tumor formation phase, *Apc*$^{Min/+}$ mice exhibit minimal, if any, visible intestinal tumors.[28] To probe this early stage, we administered tamoxifen (TMX) orally to the *AGAi14* mice, aged 4-to-5 weeks, on a daily regimen over a span of five consecutive days (Figure 4B), thereby labeling Grem1$^+$ iRSCs with tdTomato for subsequent identification of their progeny. By 12 weeks, consistent with our prior *Apc*$^{Min/+}$ studies (Figure 3), we harvested and processed the intestinal tissues as described previously. We observed that in non-tumorous regions, tdTomato$^+$ cells localized specifically below the *Sii* (Figure 4C). Conversely, within tumor regions, a substantial migration of tdTomato$^+$ cells toward the apical side was noted (Figure 4D), reminiscent of our findings of IF staining using a single *Apc*$^{Min+}$ model (Figures 3A and 3B). A panoramic view supported such a contrast in tdTomato$^+$ cell distribution between tumor and normal regions (Figure S4). Despite their proximity to epithelial cells, these cells maintained their stromal identity, as confirmed by vimentin co-staining (Figure 4E, Grem1+tdT+VIM+DAPI). Assessing whether these tdTomato$^+$ stromal cells continued to produce Grem1 as their iRSCs progenitors, we conducted multiple fluorescent stainings and found a significant overlap (appearing orange) between Grem1 (green) and tdTomato (red) expression, indicating retention of paracrine function at 12 weeks and their potential contribution to tumor progression (Figure 4E, Grem1+tdT). At this age, most Grem1$^+$ stromal cells were traced back to Grem1$^+$ iRSCs, with 92.04% showing tdTomato co-expression (Figure 4F, $p < 0.0001$; Table S3). Notably, the remaining 7.96% of tdTomato$^-$/Grem1$^+$ cells were primarily located in the submucosal layer (*S*) and also co-stained with vimentin (Figures 4E and 4G). This minor subset, distinct from the major group which originated from Grem1$^+$ iRSCs, may represent a secondary wave of Grem1 activation post-tumor initiation or during progression. Taken together, our lineage tracing in the *AGAi14* mice demonstrates that the predominant population of Grem1$^+$ stromal cells at 12 weeks arises from early-stage Grem1$^+$ iRSCs, highlighting an emerging and persistent cell population that may play a crucial role from the onset through the course of tumorigenesis.

Elucidating the heterogeneity of tdTomato$^-$/Grem1$^+$ stromal cells

α-SMA is recognized as a marker for myofibroblasts,[29,30] and in bowel diseases, the related ISEMFs have been shown to express Grem1.[24] To unveil the identity of the minority population of tdTomato$^-$/Grem1$^+$ stromal cells during tumor development, we analyzed tissue sections from 12-week-old *AGAi14* mice. Remarkably, we observed distinct α-SMA expression within the tdTomato$^-$/Grem1$^+$ stromal cells: a subset exhibited α-SMA positivity, indicative of myofibroblast-like properties, while others did not express α-SMA, suggesting alternative phenotypes (Figures 5A and 5B). The ratio of α-SMA$^+$ ISEMFs to α-SMA$^-$/tdTomato$^-$/Grem1$^+$ stromal cells within the tdTomato$^-$/Grem1$^+$ group was not significantly different (Figure 5C, $p = 0.5556$; Table S4). Nonetheless, we did not observe α-SMA expression in tdTomato$^+$/Grem1$^+$ stromal cells (Figures 5A and 5B), implying that progeny of Grem1$^+$ iRSCs may not strictly align with the myofibroblast lineage in our model. Collectively, these findings highlight the intricate heterogeneity of cell origins and potential functional diversity of the Grem1$^+$ stromal cells.

Three-dimensional (3D) rendering of two distinct Grem1$^+$ stromal cell populations within the intestinal TME

To enhance our understanding of the origins, distribution, and potential role of the two distinct Grem1$^+$ stromal cell populations within the intestinal TME, we employed 3D surface rendering to visualize tumor tissue from 12-week-old *AGAi14* mice using Imaris software (Figure 6). As expected, tumor cells showed a marked decrease in E-cadherin expression compared to the adjacent normal tissue (Figure 6A). High-resolution analysis further segregated these cell populations (Figure 6B), confirming a predominant population of tdTomato$^+$/Grem1$^+$ stromal cells, alongside a smaller group of tdTomato$^-$/Grem1$^+$ cells, in keeping with our previous observations (Figure 4). Subsequent z-stack imaging followed by 3D reconstruction facilitated detailed examination of their spatial distribution (Figure 6C). Significantly, tdTomato$^+$/Grem1$^+$ stromal cells were observed infiltrating or in close proximity to E-cadherin$^+$ tumor cells, while tdTomato$^-$/Grem1$^+$ stromal cells were more not obviously specially associated with the epithelial tumor cells (Figure 6C). These observations suggest that tdTomato$^+$/Grem1$^+$ stromal cells, likely descendants of Grem1$^+$ iRSCs, could be integral in directly mediating interactions with neoplastic cells, whereas tdTomato$^-$/Grem1$^+$ stromal cells may remain stationary pending further stimuli and/or disease progression.

DISCUSSION

In this study, we developed an improved Swiss-roll technique featuring a tailored mold that not only achieves high-quality staining results but also enables a more detailed examination of the entire gut. Employing a spontaneous intestinal tumor model (*Apc*$^{Min/+}$), we observed an increased presence of Grem1$^+$ CAFs/stromal cells within neoplastic regions. Further, utilizing a cell lineage tracing mouse model (*AGAi14*), we identified at least two distinct lineages of Grem1$^+$ CAFs, with the majority originating from Grem1$^+$ iRSCs, and a minority retaining characteristics of ISEMFs. Our results offer substantial *in vivo* evidence supporting the significance of Grem1$^+$ iRSCs as critical anti-tumor targets in the early stages of tumorigenesis.

Our innovative use of a tailored mold for longitudinal sectioning adeptly handles the challenges posed by the delicate mouse intestinal mucosa and its narrow luminal space. Using scissors to cut the intestine often results in serrated edges, which, when rolled into a Swiss roll and prepared into tissue blocks for sectioning, can lead to partial tissue loss in certain areas. In contrast, using our custom-designed device for intestinal incisions readily yields intestines with neatly trimmed edges. Preserving tissue integrity is crucial, especially in oncological studies, where a full-length view of the intestinal tumor burden is necessary. Any loss of tissue could lead to significant inaccuracies in tumor quantification, which represents a critical shortcoming. Additionally, using our tailored mold for intestinal sectioning is faster, facilitating a quicker

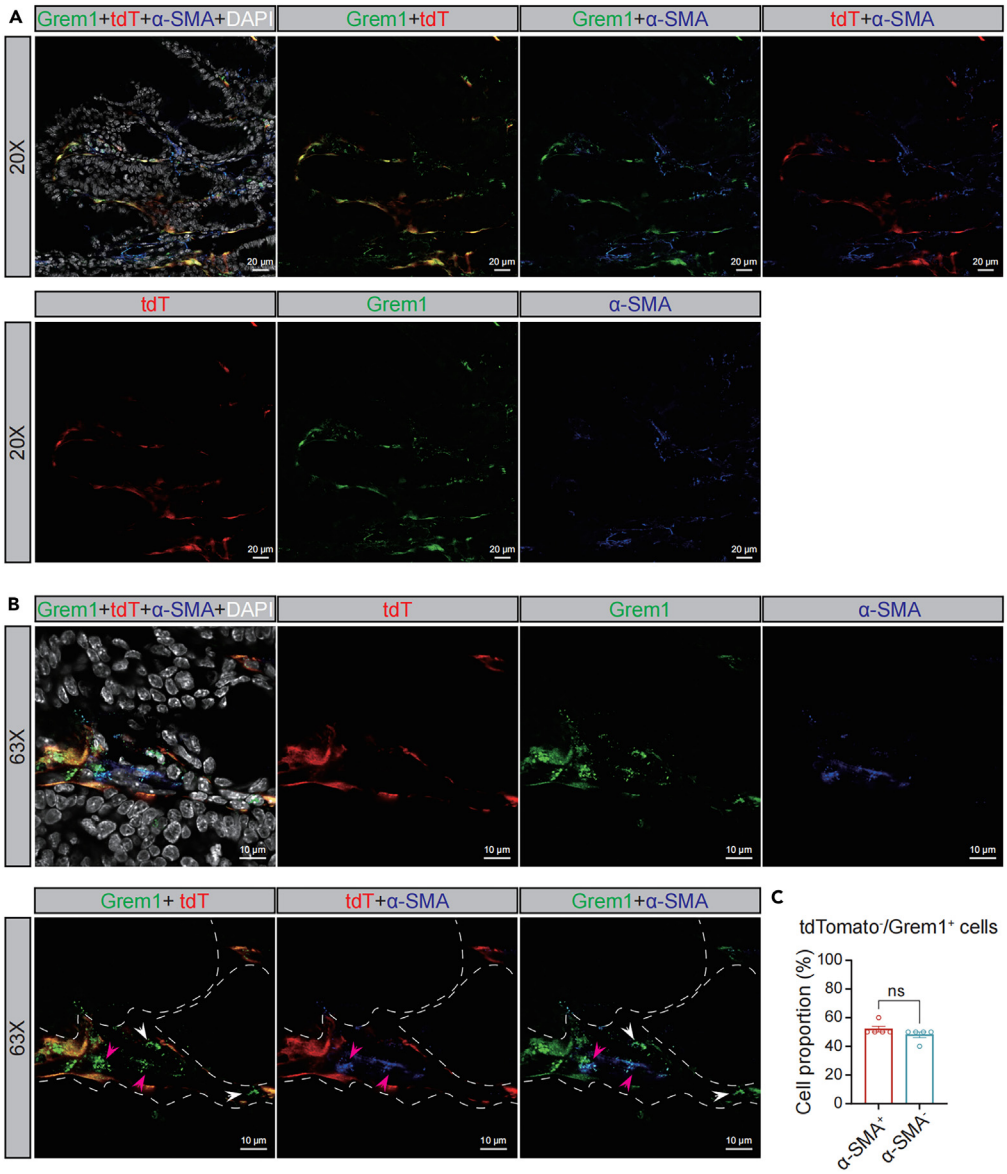

Figure 5. Elucidating the heterogeneity of tdTomato^{-}/Grem1^{+} stromal cells

(A) Representative IF staining at 20X magnification for Grem1 (green), tdTomato (red), α-SMA (blue) and DAPI (white) in the tumor area of 12-week-old *AGAi14* mice. Scale bar: 20 μm.

(B) Representative IF staining at 63X magnification for Grem1 (green), tdTomato (red), α-SMA (blue) and DAPI (white) in the tumor area of 12-week-old *AGAi14* mice. Three irregular white dashed lines delineate the epithelial regions. White arrows point to α-SMA^{-}/tdTomato^{-}/Grem1^{+} cells, while magenta arrows highlight α-SMA^{+}/tdTomato^{-}/Grem1^{+} cells. Scale bar: 10 μm.

(C) Quantitative analysis detailing the proportion of tdTomato^{-}/Grem1^{+} cells that are either α-SMA^{+} or α-SMA^{-} within the tumor region, based on 40X magnification images from intestinal sections of five *AGAi14* mice. Statistical analysis conducted with a two-tailed Mann-Whitney test yielded a *p* value of 0.5556, indicated as not significant (ns). Data are presented as the mean ± SEM.

transition to subsequent fixation steps crucial for preserving the integrity of tissue antigens. As is known, the time window for autolysis in intestinal tissue post-extraction is notably brief, underscoring the need for rapid processing.[19]

Typically, four individual tissue blocks are prepared from the four intestinal rolls of a single mouse. However, our modified method improves upon this by preparing all four intestinal rolls into one tissue block, which enhances efficiency and consistency. Unlike Sohrabi et al.'s method,[31] which prepares multiple intestinal segments from different mice using gelatin embedding, our technique uses frozen tissue from a single mouse. This holistic approach allows for a more precise and comprehensive examination of the entire intestinal landscape, offering deeper insights into the complex pathology of cancer.

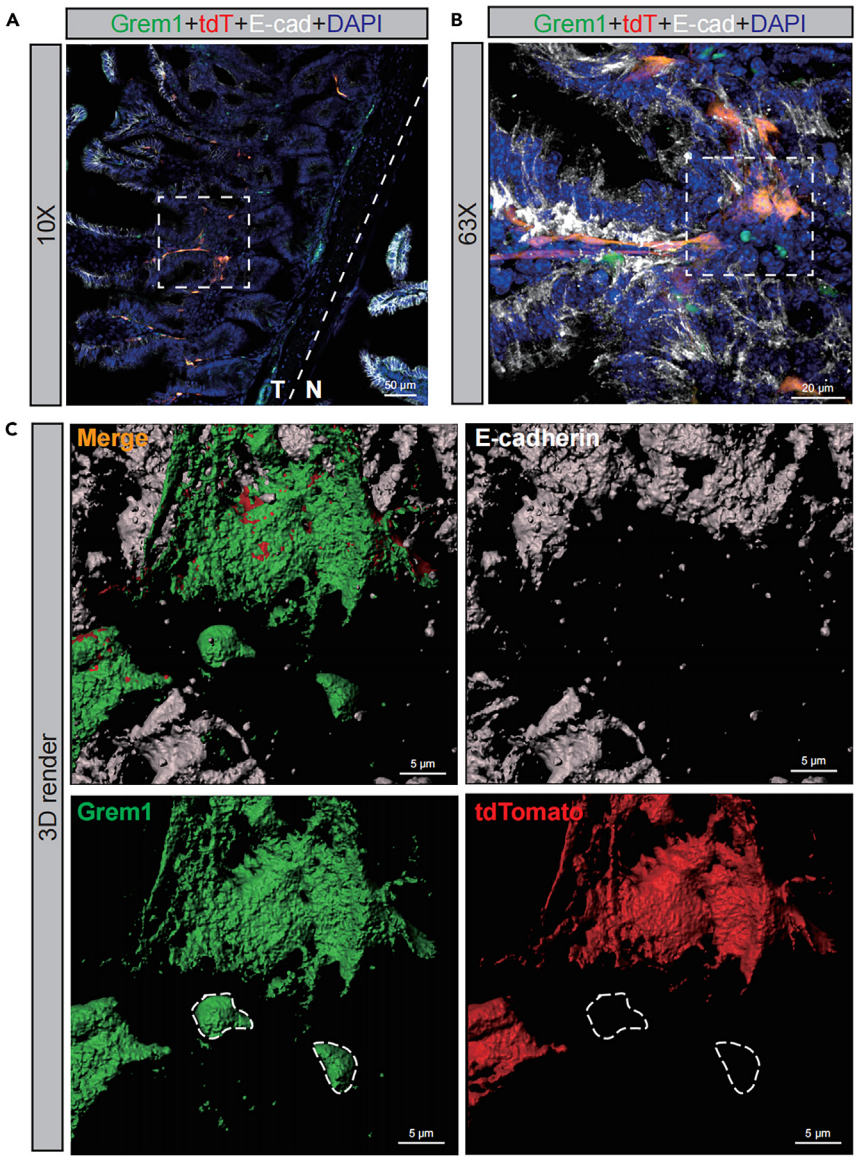

Figure 6. 3D visualization of Grem1$^+$ stromal cell diversity in the intestinal tumor microenvironment

(A) Representative IF staining at 10X magnification for Grem1 (green), tdTomato (red), E-cadherin (white) and DAPI (blue) in the tumor area of 12-week-old *AGAi14* mice. The white dotted line separates the tumor area (T) from the normal area (N). A white dashed box indicates the region magnified to 63X in panel B. Scale bar: 50 μm.

(B) Representative IF staining at 63X magnification for Grem1 (green), tdTomato (red), E-cadherin (white) and DAPI (blue) in the tumor area of 12-week-old *AGAi14* mice. A white dashed box highlights the area further enlarged in panel C. Scale bar: 20 μm.

(C) 3D reconstruction from the z-stack images obtained from panel B is rendered using Imaris software. Two white irregular dashed boxes mark tdTomato$^-$/Grem1$^+$ cells. Scale bar: 5 μm.

Paraffin embedding is indeed effective in maintaining tissue morphology; however, processes such as dehydration and high-temperature wax immersion can be detrimental to the mapping and tracing of Grem1$^+$ cells. Therefore, we adopted a frozen embedding approach. Frozen sectioning does not require high temperatures or intensive chemical treatment, and it skips the dehydration and clearing steps needed for paraffin sectioning. This method, also known as gut Swiss rolls using tailored mold and followed by frozen sectioning, keeps tissue morphology as intact as paraffin sectioning does, and even better preserves the native state of proteins and antigens, making it more suitable for IF staining. In summary, our methodological enhancement not only simplifies the tissue preparation process but also maintains the integrity and immunoreactivity of tissue antigens, which is essential for accurate histological analysis in cancer research.

The Swiss-roll technique is widely utilized in intestinal research. However, the rolled intestine configuration is not very intuitive and hinders a comprehensive understanding of the entire intestine. Recent advancements in bioimage informatics have provided innovative solutions to

the limitation. Technologies such as IntestLine[32] have emerged, enabling the processing and unrolling of imaging data from rolled intestinal tissues into a linear format. By mapping the rolled tissue onto a line, researchers can achieve clearer visualization of spatial patterns, facilitating a better understanding of the biological processes occurring along both the proximal-distal and serosa-luminal axes. Overall, combining the Swiss-roll technique with advanced bioimage informatics approaches will ensure its continued and enhanced utility in the future.

In the normal intestine, BMP signaling at the villus tips curtails cell proliferation, while Wnt signaling at the crypt base sustains stem cells and renews the epithelium. The gradient of Wnt and BMP signals along the villus-crypt axis is crucial for maintaining gut homeostasis.[33] Overexpression of Grem1, a known BMP antagonist, can disrupt this equilibrium and has been implicated in various cancers,[34–36] including CRC.[13] Kobayashi et al. have reported Grem1-expressing CAFs in CRC exert a tumor-promoting effect by inhibiting the BMP pathway.[13] Similarly, Ren et al. have also demonstrated that high GREM1 expression in CAFs contributes to a desmoplastic microenvironment that fuels breast cancer invasion.[36] In keeping, our findings indicate that Grem1$^+$ CAFs are associated with intestinal tumor progression.

While Grem1 expression is predominantly noted in stromal fibroblasts across various cancer types,[13,36,37] suggesting CAFs as a primary source of Grem1, the role of Grem1$^+$ epithelial cells should not be overlooked. Although we observed a very low number of Grem1$^+$ tumor cells from the epithelial lineage, studies have shown that aberrant GREM1 expression in epithelial cells can lead to excessive stem cell activity in hereditary mixed polyposis syndrome (HMPS).[24,38] Lan et al. revealed that in pancreatic adenocarcinoma (PDAC), Grem1 expression mainly comes from tumor cells undergoing epithelial-to-mesenchymal transition (EMT), with Grem1 being crucial for maintaining epithelial PDAC cells.[39] These findings suggest the diverse functional roles of Grem1 in tumor cells compared to CAFs.

Although extensive research has focused on the role of Grem1$^+$ CAFs during tumor progression, the origins of these cells remain poorly understood. It is unclear whether Grem1$^+$ CAFs arise from local precursors within the gut or are recruited from distant tissues such as bone marrow (BM) or adipose tissue. The characterization of Grem1$^+$ iRSCs as a subset of stromal cells possessing defining stem cell characteristics, such as self-renewal and multipotentiality, is well-documented by Worthley et al.[23] In their non-tumor transgenic mouse models, Worthley et al. conducted lineage tracing experiments that demonstrated these cells in the gut undergo continuous self-renewal and give rise to reticular, periepithelial mesenchymal lineages throughout both the crypt and villus sheaths. These Grem1$^+$ iRSCs were shown to proliferate slowly, with a continuous division and expansion process extending up to 12 months. Our lineage tracing experiments, conducted in the context of intestinal tumors, align with their findings, suggesting that Grem1$^+$ CAFs predominantly originate from Grem1$^+$ iRSCs. Remarkably, we observed a significant presence of progeny cells of Grem1$^+$ iRSCs (marked by tdTomato) within just three months in tumor areas in our *Apc*$^{Min/+}$ intestinal tumor model compared to wild-type mice (12 months).[23] This rapid expansion contrasts with the slow proliferation observed in the non-tumor context, suggesting a dynamic and responsive behavior of Grem1$^+$ iRSCs in the TME. Further, Grem1$^+$ iRSCs descendant cells exhibited pronounced migration toward the apical surfaces of the villi within the tumor regions. This observation also raises intriguing questions about the precise cellular mechanisms driving this migration.[40,41] For example, CRC cells may secrete specific cytokines to attract Grem1$^+$ CAFs toward the tumor area, which requires further investigation in the future.

Fibroblasts are known to be complex and heterogeneous, performing diverse functions in both the lamina propria of intestinal mucosa and in CRC tissues.[7,42,43] Recent studies have characterized several major CAF subtypes,[44,45] including myofibroblastic CAFs (myCAFs),[46] inflammatory CAFs (iCAFs),[47] and antigen-presenting CAFs (aCAFs).[48] In this study, we simultaneously identified a second subset of Grem1$^+$ CAFs, though limited in number, co-expressing α-SMA but not derived from iRSCs (i.e., tdTomato$^-$). Unlike the iRSCs-derived Grem1$^+$ CAFs infiltrating the tumor tissue, these Grem1$^+$ ISEMFs appear to be stationary and distant from the tumor core, potentially serving as a backup source for the primary Grem1$^+$ CAFs. In keeping, Biffi et al. provided evidence that inhibiting myCAFs does not affect primary pancreatic tumor growth, whereas inhibiting iCAFs does.[49]

We postulate that these Grem1$^+$ ISEMFs may arise from locally proliferating myCAFs or extraintestinal sources such as BM. Reports suggest that BM-derived mesenchymal stem cells, known for their self-renewal and differentiation capabilities, can transform into CAFs within the TME.[50,51] Nonetheless, further research is necessary to elucidate the origins of Grem1$^+$ ISEMFs, potentially through cell lineage tracing and/or BM transplantation experiments.

In summary, our study not only enhances the Swiss-roll technique for histological analysis, but also provides pivotal insights into the distribution and origin of Grem1$^+$ CAFs in *Apc*$^{Min/+}$ mice. Our findings open new avenues for research into the heterogeneity of Grem1$^+$ CAFs in CRC and the potential therapeutic interventions targeting early-stage Grem1$^+$ iRSCs.

Limitations of the study

Our study has several limitations. First, we are not able to observe the entire intestine using one continuous roll. While technically possible, there are several significant drawbacks. The mouse intestine can exceed 50 cm in length, making the preparation and handling of such a device impractical in a routine laboratory setting. A long stainless-steel rod is prone to folding and damage, compromising its utility and longevity. Additionally, the industrial production of a mold to accommodate such a long rod would be complex and costly. Meanwhile, we acknowledge that the removal of the cecum is a crucial step in our preparation process, as tumors do not typically develop in the cecum of mice. Furthermore, the presence of the cecum would obstruct the insertion of the rod through the intestinal lumen, further complicating the procedure. In this study, our method allows us to observe the entire intestine on a single slide. This slide contains the four rolls representing different segments of a single mouse intestine, providing a comprehensive view without the logistical challenges of handling an excessively long roll.

Second, we utilized the classical APC spontaneous intestinal adenoma model to simulate the transformation process from adenoma to adenocarcinoma. This model provides a significant perspective for understanding classical pathogenic mechanisms of CRC. However, it is crucial to acknowledge that the onset and progression of CRC involve a variety of biological pathways and mechanisms. For instance, colitis-associated cancer represents another key pathogenic model. Considering this complexity, it is important to recognize the limitations in generalizing our findings to other CRC models, such as the AOM/DSS-induced colitis-associated CRC model,[52,53] which may involve different pathogenic pathways and molecular mechanisms. Therefore, considering the specificity of different models is essential when interpreting and generalizing our research findings.

Third, our study was limited to intestinal samples collected from mice at 12 weeks of age, focusing on early to mid-stages of CRC. Consequently, our findings may not encapsulate the full spectrum of the disease, particularly the late-stage pathophysiological changes. While this does not constitute a longitudinal study and excludes the late stages of the disease, our findings offer novel insights into the early phases of CRC.

Fourth, while we have extensively investigated the primary origins/progenitors of Grem1$^+$ CAFs, specifically Grem1$^+$ iRSCs, our study did not further trace the cellular origins and characteristics of the less prevalent tdTomato$^-$/Grem1$^+$ cells, such as Grem1$^+$ ISEMFs. To address this gap, future studies will need to employ techniques such as FACS (fluorescence-activated cell sorting), scRNA sequencing (single-cell RNA sequencing), spatial transcriptomics, and additional lineage tracing mouse models. These investigations are crucial for unraveling the intricate heterogeneity inherent in Grem1$^+$ cells.

RESOURCE AVAILABILITY

Lead contact

Further information and requests for resources and reagents should be directed to and will be fulfilled by the lead contact, Ningning Li (linn29@mail.sysu.edu.cn).

Materials availability

This study did not generate new unique reagents.

Data and code availability

- All data reported in this paper will be shared by the lead contact upon request.
- This paper does not report original code.
- Any additional information required to reanalyze the data reported in this paper is available from the lead contact upon request.

ACKNOWLEDGMENTS

This study was funded by the National Natural Science Foundation of China (81874176; 82072766), Guangdong Provincial Key Laboratory of Digestive Cancer Research (2021B1212040006), the Sanming Project of Medicine in Shenzhen (SZSM202111005), and Sun Yat-sen University, Higher Education Teaching Research and Reform Project 2021 A1032 1030. We acknowledge Jia Chen and Peijia Yao from the Seventh Affiliated Hospital, Sun Yat-sen University for their contribution to performing tissue processing and 3D rendering analysis.

AUTHOR CONTRIBUTIONS

Conceptualization, Y.H.J. and N.N.L.; methodology, Z.F., Y.F.C., Q.Z., and C.X.L.; investigation, Y.M.Y., Z.R.L., Q.L.J., and Y.F.G.; resources, Q.Z., Z.P.D., and Y.F.C.; visualization, Y.H.; writing—original draft, Y.H.J. and N.N.L.; writing—review and editing, Y.H.J., Z.F., C.X.L., and N.N.L.; writing—revise, Y.H.J., Z.F., Y.F.C., Q.L.J., Q.Z., and N.N.L.; supervision, N.N.L., X.J.M., Y.L.H., Q.Z., and Q.Y.Z.; funding acquisition, N.N.L. and Y.L.H.

DECLARATION OF INTERESTS

The authors declare no competing interests.

STAR★METHODS

Detailed methods are provided in the online version of this paper and include the following:

- KEY RESOURCES TABLE
- EXPERIMENTAL MODEL AND STUDY PARTICIPANT DETAILS
  - Mice
- METHOD DETAILS
  - Collection of mouse intestinal samples and preparation of frozen Swiss rolls slides
  - Multiple frozen tissue section staining methods
  - 3D rendering
  - Microscope usage information
- QUANTIFICATION AND STATISTICAL ANALYSIS

SUPPLEMENTAL INFORMATION

Supplemental information can be found online at https://doi.org/10.1016/j.isci.2024.111173.

Received: December 4, 2023
Revised: June 18, 2024
Accepted: October 10, 2024
Published: October 15, 2024

REFERENCES

1. Siegel, R.L., Miller, K.D., Wagle, N.S., and Jemal, A. (2023). Cancer statistics, 2023. CA. Cancer J. Clin. *73*, 17–48. https://doi.org/10.3322/caac.21763.
2. de Visser, K.E., and Joyce, J.A. (2023). The evolving tumor microenvironment: From cancer initiation to metastatic outgrowth. Cancer Cell *41*, 374–403. https://doi.org/10.1016/j.ccell.2023.02.016.
3. Feng, B., Wu, J., Shen, B., Jiang, F., and Feng, J. (2022). Cancer-associated fibroblasts and resistance to anticancer therapies: status, mechanisms, and countermeasures. Cancer Cell Int. *22*, 166. https://doi.org/10.1186/s12935-022-02599-7.
4. Tsoumakidou, M. (2023). The advent of immune stimulating CAFs in cancer. Nat. Rev. Cancer *23*, 258–269. https://doi.org/10.1038/s41568-023-00549-7.
5. Zhang, H., Yue, X., Chen, Z., Liu, C., Wu, W., Zhang, N., Liu, Z., Yang, L., Jiang, Q., Cheng, Q., et al. (2023). Define cancer-associated fibroblasts (CAFs) in the tumor microenvironment: new opportunities in cancer immunotherapy and advances in clinical trials. Mol. Cancer *22*, 159. https://doi.org/10.1186/s12943-023-01860-5.
6. Lavie, D., Ben-Shmuel, A., Erez, N., and Scherz-Shouval, R. (2022). Cancer-associated fibroblasts in the single-cell era. Nat. Cancer *3*, 793–807. https://doi.org/10.1038/s43018-022-00411-z.
7. Biffi, G., and Tuveson, D.A. (2021). Diversity and Biology of Cancer-Associated Fibroblasts. Physiol. Rev. *101*, 147–176. https://doi.org/10.1152/physrev.00048.2019.
8. Brazil, D.P., Church, R.H., Surae, S., Godson, C., and Martin, F. (2015). BMP signalling: agony and antagony in the family. Trends Cell Biol. *25*, 249–264. https://doi.org/10.1016/j.tcb.2014.12.004.
9. O'Reilly, S. (2021). Gremlin: a complex molecule regulating wound healing and fibrosis. Cell. Mol. Life Sci. *78*, 7917–7923. https://doi.org/10.1007/s00018-021-03964-x.
10. Yang, Y., Zeng, Q.S., Zou, M., Zeng, J., Nie, J., Chen, D., and Gan, H.T. (2021). Targeting Gremlin 1 Prevents Intestinal Fibrosis Progression by Inhibiting the Fatty Acid Oxidation of Fibroblast Cells. Front. Pharmacol. *12*, 663774. https://doi.org/10.3389/fphar.2021.663774.
11. Park, S.A., Sung, N.J., Choi, B.J., Kim, W., Kim, S.H., and Surh, Y.J. (2020). Gremlin-1 augments the oestrogen-related receptor alpha signalling through EGFR activation: implications for the progression of breast cancer. Br. J. Cancer *123*, 988–999. https://doi.org/10.1038/s41416-020-0945-0.
12. Cheng, C., Wang, J., Xu, P., Zhang, K., Xin, Z., Zhao, H., Ji, Z., Zhang, M., Wang, D., He, Y., et al. (2022). Gremlin1 is a therapeutically targetable FGFR1 ligand that regulates lineage plasticity and castration resistance in prostate cancer. Nat. Cancer *3*, 565–580. https://doi.org/10.1038/s43018-022-00380-3.
13. Kobayashi, H., Gieniec, K.A., Wright, J.A., Wang, T., Asai, N., Mizutani, Y., Lida, T., Ando, R., Suzuki, N., Lannagan, T.R.M., et al. (2021). The Balance of Stromal BMP Signaling Mediated by GREM1 and ISLR Drives Colorectal Carcinogenesis. Gastroenterology *160*, 1224–1239.e30. https://doi.org/10.1053/j.gastro.2020.11.011.
14. Karagiannis, G.S., Musrap, N., Saraon, P., Treacy, A., Schaeffer, D.F., Kirsch, R., Riddell, R.H., and Diamandis, E.P. (2015). Bone morphogenetic protein antagonist gremlin-1 regulates colon cancer progression. Biol. Chem. *396*, 163–183. https://doi.org/10.1515/hsz-2014-0221.
15. Rycaj, K., and Tang, D.G. (2015). Cell-of-Origin of Cancer versus Cancer Stem Cells: Assays and Interpretations. Cancer Res. *75*, 4003–4011. https://doi.org/10.1158/0008-5472.CAN-15-0798.
16. Wang, L.L., Serrano, C., Zhong, X., Ma, S., Zou, Y., and Zhang, C.L. (2021). Revisiting astrocyte to neuron conversion with lineage tracing in vivo. Cell *184*, 5465–5481.e16. https://doi.org/10.1016/j.cell.2021.09.005.
17. Raposo, T.P., Alfahed, A., Nateri, A.S., and Ilyas, M. (2020). Tensin4 (TNS4) is upregulated by Wnt signalling in adenomas in multiple intestinal neoplasia (Min) mice. Int. J. Exp. Pathol. *101*, 80–86. https://doi.org/10.1111/iep.12352.
18. Sun, W., Gao, J., Yang, B., Chen, X., Kang, N., and Liu, W. (2023). Protocol for colitis-associated colorectal cancer murine model induced by AOM and DSS. STAR Protoc. *4*, 102105. https://doi.org/10.1016/j.xpro.2023.102105.
19. Pereira E Silva, A., Lourenço, A.L., Marmello, B.O., Bitteti, M., and Teixeira, G.A.P.B. (2019). Comparison of two techniques for a comprehensive gut histopathological analysis: Swiss Roll versus Intestine Strips. Exp. Mol. Pathol. *111*, 104302. https://doi.org/10.1016/j.yexmp.2019.104302.
20. Reilly, R.W., and Kirsner, J.B. (1965). Runt Intestinal Disease. Lab. Invest. *14*, 102–107.
21. Le Naour, J., Montégut, L., Joseph, A., Garbin, K., Vacchelli, E., Kroemer, G., Pol, J.G., and Maiuri, M.C. (2022). Improved Swiss-rolling method for histological analyses of colon tissue. MethodsX *9*, 101630. https://doi.org/10.1016/j.mex.2022.101630.
22. Park, C.M., Reid, P.E., Walker, D.C., and MacPherson, B.R. (1987). A simple, practical 'swiss roll' method of preparing tissues for paraffin or methacrylate embedding. J. Microsc. *145*, 115–120. https://doi.org/10.1111/j.1365-2818.1987.tb01321.x.
23. Worthley, D.L., Churchill, M., Compton, J.T., Tailor, Y., Rao, M., Si, Y., Levin, D., Schwartz, M.G., Uygur, A., Hayakawa, Y., et al. (2015). Gremlin 1 identifies a skeletal stem cell with bone, cartilage, and reticular stromal potential. Cell *160*, 269–284. https://doi.org/10.1016/j.cell.2014.11.042.
24. Jaeger, E., Leedham, S., Lewis, A., Segditsas, S., Becker, M., Cuadrado, P.R., Davis, H., Kaur, K., Heinimann, K., Howarth, K., et al. (2012). Hereditary mixed polyposis syndrome is caused by a 40-kb upstream duplication that leads to increased and ectopic expression of the BMP antagonist GREM1. Nat. Genet. *44*, 699–703. https://doi.org/10.1038/ng.2263.
25. Yamabayashi, S. (1987). Periodic acid-Schiff-alcian blue: a method for the differential staining of glycoproteins. Histochem. J. *19*, 565–571. https://doi.org/10.1007/BF01687364.
26. Hu, J., Huang, H., Che, Y., Ding, C., Zhang, L., Wang, Y., Hao, H., Shen, H., and Cao, L. (2021). Qingchang Huashi Formula attenuates DSS-induced colitis in mice by restoring gut microbiota-metabolism homeostasis and goblet cell function. J. Ethnopharmacol. *266*, 113394. https://doi.org/10.1016/j.jep.2020.113394.
27. Ren, J., Sui, H., Fang, F., Li, Q., and Li, B. (2019). The application of Apc(Min/+) mouse model in colorectal tumor researches. J. Cancer Res. Clin. Oncol. *145*, 1111–1122. https://doi.org/10.1007/s00432-019-02883-6.
28. Babaei-Jadidi, R., Li, N., Saadeddin, A., Spencer-Dene, B., Jandke, A., Muhammad, B., Ibrahim, E.E., Muraleedharan, R., Abuzinadah, M., Davis, H., et al. (2011). FBXW7 influences murine intestinal homeostasis and cancer, targeting Notch, Jun, and DEK for degradation. J. Exp. Med. *208*, 295–312. https://doi.org/10.1084/jem.20100830.
29. Kalluri, R., and Zeisberg, M. (2006). Fibroblasts in cancer. Nat. Rev. Cancer *6*, 392–401. https://doi.org/10.1038/nrc1877.
30. Hinz, B., Phan, S.H., Thannickal, V.J., Galli, A., Bochaton-Piallat, M.L., and Gabbiani, G. (2007). The myofibroblast: one function, multiple origins. Am. J. Pathol. *170*, 1807–1816. https://doi.org/10.2353/ajpath.2007.070112.
31. Sohrabi, M., and Combs, C.K. (2019). A protocol for making and sectioning multiple embedded Swiss-rolls in a gelatin matrix. MethodsX *6*, 2028–2036. https://doi.org/10.1016/j.mex.2019.08.021.
32. Yuzeir, A., Bejarano, D.A., Grein, S., Hasenauer, J., Schlitzer, A., and Yu, J. (2023). IntestLine: a shiny-based application to map the rolled intestinal tissue onto a line. Bioinformatics *39*, btad140. https://doi.org/10.1093/bioinformatics/btad140.
33. Qi, Z., Li, Y., Zhao, B., Xu, C., Liu, Y., Li, H., Zhang, B., Wang, X., Yang, X., Xie, W., et al. (2017). BMP restricts stemness of intestinal Lgr5(+) stem cells by directly suppressing their signature genes. Nat. Commun. *8*, 13824. https://doi.org/10.1038/ncomms13824.
34. Wu, Z., Liu, R., Miao, X., Li, D., Zou, Q., Yuan, Y., and Yang, Z. (2020). Prognostic and clinicopathological significance of Hapto and Gremlin1 expression in extrahepatic cholangiocarcinoma. J. Cancer *11*, 199–207. https://doi.org/10.7150/jca.36886.
35. Sato, M., Kawana, K., Fujimoto, A., Yoshida, M., Nakamura, H., Nishida, H., Inoue, T., Taguchi, A., Takahashi, J., Adachi, K., et al. (2016). Clinical significance of Gremlin 1 in cervical cancer and its effects on cancer stem cell maintenance. Oncol. Rep. *35*, 391–397. https://doi.org/10.3892/or.2015.4367.

36. Ren, J., Smid, M., Iaria, J., Salvatori, D.C.F., van Dam, H., Zhu, H.J., Martens, J.W.M., and Ten Dijke, P. (2019). Cancer-associated fibroblast-derived Gremlin 1 promotes breast cancer progression. Breast Cancer Res. *21*, 109. https://doi.org/10.1186/s13058-019-1194-0.
37. Kim, H.S., Shin, M.S., Cheon, M.S., Kim, J.W., Lee, C., Kim, W.H., Kim, Y.S., and Jang, B.G. (2017). GREM1 is expressed in the cancer-associated myofibroblasts of basal cell carcinomas. PLoS One *12*, e0174565. https://doi.org/10.1371/journal.pone.0174565.
38. Davis, H., Irshad, S., Bansal, M., Rafferty, H., Boitsova, T., Bardella, C., Jaeger, E., Lewis, A., Freeman-Mills, L., Giner, F.C., et al. (2015). Aberrant epithelial GREM1 expression initiates colonic tumorigenesis from cells outside the stem cell niche. Nat. Med. *21*, 62–70. https://doi.org/10.1038/nm.3750.
39. Lan, L., Evan, T., Li, H., Hussain, A., Ruiz, E.J., Zaw Thin, M., Ferreira, R.M.M., Ps, H., Riising, E.M., Zen, Y., et al. (2022). GREM1 is required to maintain cellular heterogeneity in pancreatic cancer. Nature *607*, 163–168. https://doi.org/10.1038/s41586-022-04888-7.
40. Tu, Z., and Karnoub, A.E. (2022). Mesenchymal stem/stromal cells in breast cancer development and management. Semin. Cancer Biol. *86*, 81–92. https://doi.org/10.1016/j.semcancer.2022.09.002.
41. Ma, X., Chen, J., Liu, J., Xu, B., Liang, X., Yang, X., Feng, Y., Liang, X., and Liu, J. (2021). IL-8/CXCR2 mediates tropism of human bone marrow-derived mesenchymal stem cells toward CD133(+)/CD44(+) Colon cancer stem cells. J. Cell. Physiol. *236*, 3114–3128. https://doi.org/10.1002/jcp.30080.
42. Deng, L., Jiang, N., Zeng, J., Wang, Y., and Cui, H. (2021). The Versatile Roles of Cancer-Associated Fibroblasts in Colorectal Cancer and Therapeutic Implications. Front. Cell Dev. Biol. *9*, 733270. https://doi.org/10.3389/fcell.2021.733270.
43. Lendahl, U., Muhl, L., and Betsholtz, C. (2022). Identification, discrimination and heterogeneity of fibroblasts. Nat. Commun. *13*, 3409. https://doi.org/10.1038/s41467-022-30633-9.
44. Kennel, K.B., Bozlar, M., De Valk, A.F., and Greten, F.R. (2023). Cancer-Associated Fibroblasts in Inflammation and Antitumor Immunity. Clin. Cancer Res. *29*, 1009–1016. https://doi.org/10.1158/1078-0432.CCR-22-1031.
45. Cords, L., Engler, S., Haberecker, M., Rüschoff, J.H., Moch, H., de Souza, N., and Bodenmiller, B. (2024). Cancer-associated fibroblast phenotypes are associated with patient outcome in non-small cell lung cancer. Cancer Cell *42*, 396–412.e5. https://doi.org/10.1016/j.ccell.2023.12.021.
46. Mucciolo, G., Araos Henriquez, J., Jihad, M., Pinto Teles, S., Manansala, J.S., Li, W., Ashworth, S., Lloyd, E.G., Cheng, P.S.W., Luo, W., et al. (2024). EGFR-activated myofibroblasts promote metastasis of pancreatic cancer. Cancer Cell *42*, 101–118.e111. https://doi.org/10.1016/j.ccell.2023.12.002.
47. Chen, H., Yang, W., Xue, X., Li, Y., Jin, Z., and Ji, Z. (2022). Integrated Analysis Revealed an Inflammatory Cancer-Associated Fibroblast-Based Subtypes with Promising Implications in Predicting the Prognosis and Immunotherapeutic Response of Bladder Cancer Patients. Int. J. Mol. Sci. *23*, 15970. https://doi.org/10.3390/ijms232415970.
48. Elyada, E., Bolisetty, M., Laise, P., Flynn, W.F., Courtois, E.T., Burkhart, R.A., Teinor, J.A., Belleau, P., Biffi, G., Lucito, M.S., et al. (2019). Cross-Species Single-Cell Analysis of Pancreatic Ductal Adenocarcinoma Reveals Antigen-Presenting Cancer-Associated Fibroblasts. Cancer Discov. *9*, 1102–1123. https://doi.org/10.1158/2159-8290.CD-19-0094.
49. Biffi, G., Oni, T.E., Spielman, B., Hao, Y., Elyada, E., Park, Y., Preall, J., and Tuveson, D.A. (2019). IL1-Induced JAK/STAT Signaling Is Antagonized by TGFbeta to Shape CAF Heterogeneity in Pancreatic Ductal Adenocarcinoma. Cancer Discov. *9*, 282–301. https://doi.org/10.1158/2159-8290.CD-18-0710.
50. Quante, M., Tu, S.P., Tomita, H., Gonda, T., Wang, S.S.W., Takashi, S., Baik, G.H., Shibata, W., Diprete, B., Betz, K.S., et al. (2011). Bone marrow-derived myofibroblasts contribute to the mesenchymal stem cell niche and promote tumor growth. Cancer Cell *19*, 257–272. https://doi.org/10.1016/j.ccr.2011.01.020.
51. Raz, Y., Cohen, N., Shani, O., Bell, R.E., Novitskiy, S.V., Abramovitz, L., Levy, C., Milyavsky, M., Leider-Trejo, L., Moses, H.L., et al. (2018). Bone marrow-derived fibroblasts are a functionally distinct stromal cell population in breast cancer. J. Exp. Med. *215*, 3075–3093. https://doi.org/10.1084/jem.20180818.
52. Gobert, A.P., Latour, Y.L., Asim, M., Barry, D.P., Allaman, M.M., Finley, J.L., Smith, T.M., McNamara, K.M., Singh, K., Sierra, J.C., et al. (2022). Protective Role of Spermidine in Colitis and Colon Carcinogenesis. Gastroenterology *162*, 813–827.e8. https://doi.org/10.1053/j.gastro.2021.11.005.
53. Guo, C., Guo, D., Fang, L., Sang, T., Wu, J., Guo, C., Wang, Y., Wang, Y., Chen, C., Chen, J., et al. (2021). Ganoderma lucidum polysaccharide modulates gut microbiota and immune cell function to inhibit inflammation and tumorigenesis in colon. Carbohydr. Polym. *267*, 118231. https://doi.org/10.1016/j.carbpol.2021.118231.
54. Werner, L., Müller-Fielitz, H., Ritzal, M., Werner, T., Rossner, M., and Schwaninger, M. (2012). Involvement of doublecortin-expressing cells in the arcuate nucleus in body weight regulation. Endocrinology *153*, 2655–2664. https://doi.org/10.1210/en.2011-1760.
55. Oshima, M., Oshima, H., Kitagawa, K., Kobayashi, M., Itakura, C., and Taketo, M. (1995). Loss of Apc heterozygosity and abnormal tissue building in nascent intestinal polyps in mice carrying a truncated Apc gene. Proc. Natl. Acad. Sci. USA *92*, 4482–4486. https://doi.org/10.1073/pnas.92.10.4482.

STAR★METHODS

KEY RESOURCES TABLE

REAGENT or RESOURCE	SOURCE	IDENTIFIER
Antibodies		
Goat anti-Grem1	R&D Systems	Cat#AF956; RRID: AB_2113296
Rabbit anti-E-cadherin	Cell Signaling Technology	Cat#3195; RRID: AB_2291471
Rabbit anti-Vimentin	Cell Signaling Technology	Cat#5741; RRID: AB_10695459
Rabbit anti-α-SMA	Abcam	Cat#ab5694; RRID: AB_2223021
Donkey anti-Goat IgG (H&L) Alexa Fluor 488	Abcam	Cat#ab150129; RRID: AB_2687506
Goat anti-Rabbit IgG (H&L) Alexa Fluor 647	Invitrogen	Cat#A-21244; RRID: AB_2535812
Software and algorithms		
GraphPad Prism (v9)	GraphPad Software	RRID: SCR_002798
Imaris	Imaris Software	RRID: SCR_007370
ImageJ	ImageJ Software	RRID: SCR_003070
Other		
A tailored mold 'Mouse Intestinal Longitudinal Cutting Matrix'	This paper	N/A

EXPERIMENTAL MODEL AND STUDY PARTICIPANT DETAILS

Mice

All animal experiments were approved by the Ethical Committee of Sun Yat-sen University (approval no. SYSU-IACUC-2024-001619). *Grem1-CreER^{T2}* mice (Jackson laboratories strain 027039)[23] and *Ai14* tdTomato reporter (Jackson laboratories strain 007914) mice[54] were purchased from Jackson Laboratory. *Apc$^{Min/+}$* (stock no. 002020) mice[55] were obtained from the Gempharmatech Co., Ltd. Female wild-type C57BL/6J mice were crossed with *Apc$^{Min/+}$* males to breed the male *Apc$^{Min/+}$* mice that we used for the experiments. In order to obtain *Apc$^{Min/+}$*; *Grem1-CreER^{T2}*; *Ai14* (*AGAi14*) mice, male *Grem1-CreER^{T2}* mice were initially crossed with female *Ai14* mice to achieve tdTomato labeling driven by GREM1. Female *Grem1-CreER^{T2}*; *Ai14* mice were then crossed with *Apc$^{Min/+}$* males to breed the male *AGAi14* mice that we used for the experiments. To ascertain the genotypes of various alleles, specific sets of primers were used for PCR amplification. For the *Grem1-CreER^{T2}* allele, four primers were employed: 23812 (5′-CTGTGTCGAATTACTCAGTTTGATG-3′), oIMR7338 (5′-CTAGGCCACA GAATTGAAAGATCT-3′), oIMR7339 (5′-GTAGGTGGAAATTCTAGCATCATCC-3′), and oIMR9074 (5′-AGGCAAATTTTGGTGTACGG-3′). In the case of *Apc$^{Min/+}$*, the primer pair used was 3′-ATACTACGGTATTGCCCAGC-5′ and 5′-TGTTGTTGGATGGTAAGCAC-3′. For the *Ai14* line, wild-type and mutant genotypes were differentiated using primer pairs 3′-AAGGGAGCTGCAGTGGAGTA-5′ and 5′-CCGAA AATCTGTGGGAAGTC-3′ for wild-type, and 3′-CTGTTCCTGTACGGCATGG-5′ and 5′-GGCATTAAAGCAGCGTATCC-3′ for the mutant allele. At the age of 4–5 weeks, tamoxifen (TMX) was administered by oral gavage (dissolved in corn oil at a concentration of 20 mg/mL, and administered a dose of approximately 100 mg/kg body weight) for five consecutive days. All mice were maintained on a 12-h light/dark cycle and provided with an ample supply of food and water. Subsequently, all mice were sacrificed at the age of 12 weeks, and their intestinal tissues were harvested.

METHOD DETAILS

Collection of mouse intestinal samples and preparation of frozen Swiss rolls slides

Preparation before intestinal tissue collection

Remove mouse food one night prior to intestinal tissue collection, while allowing free access to drinking water. Note: Mice typically feed at night, removing food one night in advance effectively reduces the content of the intestinal tract.

Mice anesthesia, abdominal skin preparation, and euthanasia

Mouse weighing and anesthesia induction were performed by intraperitoneal injection of 2% pentobarbital sodium (50 μL per 20 g body weight of mice). Monitor changes in reflex activity to assess the depth of anesthesia. Subsequent procedures were initiated once the mice were fully anesthetized (confirmed by the absence of a response when squeezing the mouse's toes with fingers). An electric animal hair clipper was used to shave the abdominal fur of the mice. The advantage of using automated equipment is its convenience and efficiency; however, it is also possible to use scissors for hair removal, although this method requires skill and is more time-consuming. Alternatively, the simplest method is to wet the abdominal fur with water. Note: The choice of method may vary based on the operator's experience and expertise.

Regardless of the method used, the goal is to minimize the potential interference caused by abdominal fur during dissection, such as adhesion to abdominal organs, to facilitate the dissection process. If liver or lung tissue is not required at this point (as it necessitates the step of cardiac perfusion), mouse euthanasia can be performed using the cervical dislocation method.

Mouse intestinal tissue collection

Place a disposable surgical drape on the dissection board (or a clean foam board). Secure the mouse to the dissection board using a needle or tape. Using non-dominant hand, lift the skin at the midline of the abdomen with forceps (be cautious not to grasp too deeply, avoiding unintentional injury to internal organs, especially the intestines). With the dominant hand, use dissection scissors to make a small 'V'-shaped incision at the midline of the abdomen. Extend the incision upwards to the sternum and downwards to the pubic bone to create an access for further procedures. Once the abdominal cavity is exposed, locate the stomach and identify the junction with the esophagus. Then, cut it just above the cardia. With the non-dominant hand, grasp the cut end with forceps, starting with the stomach, and carefully free the stomach and intestines from the abdominal cavity. During this process, it's essential to note that the non-dominant hand should apply moderate tension when pulling the cut end (here, it's crucial to pay attention to the force: excessive force can lead to sudden detachment of the gastrointestinal tract during the freeing process, while insufficient force won't maintain tension, affecting the efficiency of detachment). The dominant hand, holding another pair of forceps, assists in the separation of relevant mesentery and connective tissues, such as omental fat. Another important aspect not to overlook during the freeing process is to rinse the stomach and intestines that have been freed from the abdominal cavity with ice-cold PBS to keep them cold and moist at all times. In multiple practices, we found a technique during the freeing process: moisten sterile gauze with ice-cold PBS and place it on a cold board. Because the mouse's intestines are relatively long, as we gradually detach the stomach and intestines from the abdominal cavity, we can place the previously freed front portion of the gastrointestinal tissue on the moist gauze. The advantage of this operation is to keep the isolated gastrointestinal tissue continuously moist and at a low temperature. The non-dominant hand should move the grasped part while pulling the intestine, continuously toward the distal end, to maintain proper tension. Sustained and moderate tension facilitates the smooth progress of the detachment process. After completely freeing the entire gastrointestinal tract from the abdominal cavity, immediately immerse it in ice-cold PBS in a 10-cm culture dish. Note: Pour sufficient ice-cold PBS into the 10-cm culture dish and then place the culture dish on a cold plate to maintain a low temperature.

Segmentation of the mouse intestine and flushing of intestinal contents

Place sterile gauze moistened with ice-cold PBS on the work surface. Position the gastrointestinal tract from the culture dish on the sterile gauze, and use a ruler to measure and record the lengths of the small intestine and large intestine. Subsequently, divide the small intestine into three equal segments along its length, from the stomach side to the cecum side, and label them as SB1, SB2, SB3 (SB: Small Bowel). The large intestine remains as a single segment (the cecum is removed, leaving the colon and rectum), labeled as LB (LB: Large Bowel). Note: The excised stomach and cecum may be preserved or further processed based on the project's requirements. Use a simple flushing tube filled with ice-cold PBS to flush the intestinal contents. After flushing out the feces, immediately place the intestines in a new culture dish filled with ice-cold PBS. The simple flushing tube we used is a custom design, with a body of a 10-mL syringe, and the tip is made by cutting the tip of a scalpel needle.

Utilizing a tailored 'Mouse Intestinal Longitudinal Cutting Matrix' for longitudinal sectioning of the intestine

After completing the flushing of intestinal contents, the longitudinal sectioning of the intestine will be performed. In our case, we utilize a tailored 'Mouse Intestinal Longitudinal Cutting Matrix'. The mold comprises three main components: a black base, four stainless steel rods, and a silver-toned stainless-steel lid. Soak precut absorbent paper 'a' (approximately 15 cm × 8.5 cm) in ice-cold PBS and place it on the black base. Depending on personal preference, use forceps or handle it by hand to pass the four stainless steel rods through the lumens of SB1, SB2, SB3, and LB. Subsequently, secure these four stainless steel rods in order on the base, and then cover with the lid. The non-dominant hand holds the end of the intestinal tube steady with forceps, and the dominant hand holds a sterile surgical blade, using the two side walls in the middle of the lid as a fulcrum to smoothly incise the intestinal tube along the longitudinal axis, exposing the intestinal epithelium (i.e., the mucosal surface of the intestine). Note: After the surgical blade passes through the intestinal tube, a portion of it may stick to the stainless-steel rods without spreading out flat. In such cases, a 10-mL syringe can be used to spray ice-cold PBS in the direction of the surgical blade incision to help the incised intestinal tube spread out on the moist absorbent paper 'a'. Carefully remove the stainless-steel rods. At this point, the serosal surface of the intestine (i.e., the opposite side of the intestinal mucosal surface) is in close contact with the absorbent paper 'a'. Furthermore, you can observe the well-defined edge of the longitudinal intestinal section.

Rolling, fixation, and dehydration of the intestine, and preparation of frozen Swiss roll blocks

Cut one corner of another equally-sized absorbent paper 'b' at the upper right, soak it in ice-cold PBS, and then place it over the incised intestine. As a result, the four incised intact intestinal tissue pieces are sandwiched between these two absorbent papers. Note: The purpose of distinguishing between the two absorbent papers is to quickly and directly identify the mucosal and serosal surfaces of the intestine, which is instructive for the subsequent rolling direction of the Swiss roll. Roll up these two perfectly aligned absorbent papers along their longitudinal axis. Place the rolled absorbent papers in 50-mL centrifuge tubes filled with freshly prepared 4% PFA (Note: The volume of the fixation solution should be at least ten times the tissue volume, and here, we can fill the 50-mL centrifuge tubes). Allow fixation at room temperature for

24 h. Note: Ensure the use of freshly prepared fixation solution to achieve optimal fixation. Additionally, label each centrifuge tube with an alcohol-resistant marker. After 24 h of fixation, replace the 4% PFA with a 15% sucrose solution for dehydration over 24 h. Then, replace the 15% sucrose solution with a 30% sucrose solution and continue dehydration for another 24 h. After 24 h of dehydration in the 30% sucrose solution, remove the absorbent papers from the 50-mL centrifuge tubes and lay them flat on the work surface with the 'b' side facing up. Carefully unfold absorbent paper 'b' to expose the mucosal surface of the intestine. Hold the most anterior end of the intestine with curved forceps in your dominant hand, while your non-dominant hand gently grasps the most distal end with another pair of forceps or by hand. Roll up the fixed and hardened intestine with the mucosal surface facing inward, in a direction of coiling. While rolling the intestine, ensure the alignment of tissue edges to maintain the integrity of the spiral intestine roll for subsequent sectioning. After rolling the intestine into a tube, pierce it through with a 30G needle to prevent it from unraveling. Subsequently, carefully release the forceps to separate it from the intestinal roll. Note: While rolling the intestine, maintain an appropriate tension; insufficient force may lead to loss of the coiled shape, while excessive force may cause the intestine to break. Additionally, excessive tension resulting in a tightly coiled intestine may compress the villi, leading to morphological distortion, which is not conducive to calculating the villus/crypt ratio. At this point, carefully remove the 30G needle and place the four intestinal rolls in an upright position in the tissue embedding cassette in the corresponding order. Note: To ensure complete embedding with O.C.T. without compressing their form, use an embedding cassette with sufficient depth (the depth of the embedding cassette we used was 1.2 cm). Completely encase the four intestinal rolls with O.C.T., ensuring no air bubbles are formed. Then, place them on the freezing stage of the cryostat for rapid freezing. Once the O.C.T. turns white and hard, you can proceed with the subsequent sectioning steps or store them at −80°C for later use.

Preparation of frozen Swiss roll sections

Start the frozen tissue sectioning machine, adjust parameters (e.g., temperature, section thickness), and install a clean, sharp disposable blade. Apply a layer of O.C.T. onto the sample holder, place the frozen tissue block on it, and add a sufficient amount of O.C.T. on top of the tissue block for trimming during rough cutting. Then, place the sample holder on the freezing stage for rapid freezing. Secure the sample holder on the slicer. Perform rough cutting to adjust the orientation of the sample holder and position the anti-roll plate. After trimming to create a flat surface, proceed with formal sectioning. Select a section thickness as needed, typically 5–30 μm. After cutting each tissue section, gently flatten any curled portions with a fine brush before lifting the anti-roll plate. Place a clean adhesive glass slide flat above the tissue section. The tissue section will quickly adhere to the glass slide. Ensure the section is fully attached before moving on to the next cut. Note: Keep adhesive glass slides at room temperature before use; do not place them inside the cryostat, as tissue adhesion depends on the temperature difference. Frozen tissue sections containing the entire length of the mouse intestine are now prepared and can be stored at −20°C for future use.

Multiple frozen tissue section staining methods

H&E staining

Retrieve the selected frozen sections from storage at −20°C and allow them to thaw at room temperature for 10 min. Subsequently, rinse the sections with tap water again for 2 min. Stain the sections with hematoxylin solution for 20 s, adjusting the duration based on staining results if necessary. Follow this by rinsing the sections with tap water for 2 min. Next, differentiate the sections in a 1% hydrochloric acid ethanol solution for 5 s. Proceed to rinse the sections with tap water for 2 min, followed by a final rinse with distilled water for 2 min. Subsequently, stain the sections with eosin staining solution for 40 s (adjusting the duration as needed based on staining results). Rinse the sections again with tap water for 2 min. Dehydrate the sections twice in 95% ethanol, each step lasting 2 min. Finish the dehydration with fresh anhydrous ethanol for an additional 2 min. Clear the sections in xylene three times, each for 5 min. Finally, mount the sections with neutral resin.

AB-PAS staining

The following procedures were performed according to the instructions of the AB-PAS staining kit (Yeasen Biotechnology, Shanghai, China). In summary, begin by retrieving the frozen tissue sections from storage at −20°C and allowing them to thaw at room temperature for 10 min. Once thawed, submerge the tissue sections in an Alcian blue staining solution for 5 min, followed by a 2-min rinse with tap water. Next, immerse the sections in periodic acid solution for 5 min, followed by a 2-min rinse in tap water, succeeded by another 2-min rinse in distilled water. Place the sections in Schaeffer-Fulton stain solution for light-tight staining for 5 min, followed by a 5-min rinse in tap water. Subsequently, soak the sections in hematoxylin stain solution for 10 s, followed by a 2-min rinse in tap water. After that, differentiate the sections in an acid differentiation solution for 5 s, followed by a 2-min rinse in tap water. Briefly blue the sections in Scott's blueing solution, followed by a 3-min rinse in tap water. The sections are then transferred sequentially to absolute ethanol I, II, and III, each for 5 min. Subsequently, place the sections in xylene I for 5 min and then in xylene II for 5 min. Finally, after mounting the sections with neutral resin, allow the slides to air dry overnight.

IF staining

Retrieve the chosen frozen sections from −20°C and allow them to thaw at room temperature for 10 min. Subsequently, rinse the sections with PBS for 3 min, repeating this step three times on a shaker. Following, rinse the sections three times with PBS for 3 min each. Incubate the tissue sections in a blocking solution (500 μL normal donkey serum, 9.5 mL PBS, and 30 μL Triton X-100) for 1 h to block endogenous peroxidase

activity and reduce non-specific binding. Subsequent to blocking, apply the primary antibody and place the sections in a humid chamber, incubating overnight at 4°C (see key resources table for primary antibody information). The next day, remove the humid chamber from the 4°C refrigerator and allow it to equilibrate at room temperature for 30 min to 1 h. Upon equilibration, wash the tissue sections with PBS five times, each time for 5 min. Apply the secondary antibody to the sections in a light-protected environment and incubate at room temperature for 1 h (see key resources table for secondary antibody information). After incubation, wash the sections three times with PBST for 30 min each, ensuring that all steps are conducted in a light-protected environment. For improved results, we may increase the number of washes to five times, 20 min each. Please note that these steps should be executed in a light-protected environment. Mount the sections with an appropriate amount of 4′,6-diamidino-2-fenylindool (DAPI) solution and store them at room temperature overnight, then transfer to a dark environment at −20°C for long-term storage.

3D rendering

3D confocal images were taken with a ZEISS LSM880 confocal microscope (Jena, Germany) using a 63X lens. Images were smoothed and background subtracted for each channel using ImageJ software. Using Imaris software, we applied the default settings for Surface creation, setting surface detail to 0 μm and using absolute intensity for thresholding. We then selected the corresponding Surface objects to examine their spatial relationships and precisely determine the overlap within the E-cadherin, Grem1, and tdTomato channels. Finally, we utilized Imaris to generate rendered images, providing a clear 3D representation of the effects in the E-cadherin, Grem1, and tdTomato channels.

Microscope usage information

IF staining images not requiring 3D rendering were captured using a ZEISS LSM880 or 980 confocal microscopes (Jena, Germany). Additionally, panoramic views of H&E, AB-PAS, and IF staining were obtained with a Digital Pathology Scanner (KF-FL-020) from KONFOONG BIOINFORMATION TECH CO., LTD (KFBIO).

QUANTIFICATION AND STATISTICAL ANALYSIS

All experiments were performed on at least three mice per group. Grem1, E-cadherin, vimentin, α-SMA, and tdTomato-positive cells were counted in 40X images. Data are presented as the mean ± standard error of the mean (SEM). GraphPad Prism (v9) was used for statistical analyses. Unpaired, two-tailed Student's t-tests or Mann-Whitney tests were performed to analyze p values for single comparisons between two groups. Statistical significance was accepted when $p < 0.05$.